Journal of Zhejiang University-SCIENCE A 2026 27(4):334-347
www.jzus.zju.edu.cn; www.springer.com/journal/11582
E-mail: jzus_a@zju.edu.cn

Research Article
https://doi.org/10.1631/jzus.A2500379

Check for updates

Two-photon polymerization based microfluidic biochip incorporating a herringbone microchannel and deterministic lateral displacement design for efficient capture of circulating tumor cells

Xinyi LIANG[1,2*], Changwei QIN[1,2*], Kaiqiang LI[3], An REN[1,2], Jiarui HU[1,2], Weikang LV[1,2], Lunan KE[1,2], Zhen WANG[3], Mengfei YU[4], Xiuxiu JIANG[5], Huayong YANG[1,2], Xiaobin XU[6]✉, Liang MA[1,2]✉

[1]*State Key Laboratory of Fluid Power and Mechatronic Systems, Zhejiang University, Hangzhou 310058, China*
[2]*School of Mechanical Engineering, Zhejiang University, Hangzhou 310058, China*
[3]*Center for Laboratory Medicine, Allergy Center, Department of Transfusion Medicine, Zhejiang Provincial People's Hospital, Affiliated People's Hospital, Hangzhou Medical College, Hangzhou 310014, China*
[4]*The Affiliated Stomatologic Hospital, School of Medicine, Zhejiang University, Hangzhou 310003, China*
[5]*Zhejiang Provincial Clinical Research Center for Gynecology, Zhejiang Key Laboratory of Maternal and Infant Health, Department of Family Planning, Women's Hospital, Zhejiang University School of Medicine, Hangzhou 310006, China*
[6]*School of Materials Science of Engineering, Tongji University, Shanghai 201804, China*

Abstract: Circulating tumor cells (CTCs) are cells that become detached from a primary tumor and enter the vascular or lymphatic system. These cells contain nearly the entire genetic information of the primary tumor. Enrichment and detection of CTCs play a crucial role in prognostications and risk assessments of tumor metastasis and recurrence, evaluation of efficacy and potential medications for precision tumor therapy, and detection of dynamic biomarkers during tumor treatment. Current methods of CTC capture often face the challenge of balancing capture rate and purity. To address these issues, we propose a microfluidic biochip based on the principle of immunoaffinity, which incorporates a herringbone microchannel and deterministic lateral displacement (DLD) technology for the capture of CTCs. By manipulating the internal structural design of the microfluidic chip, we optimized the flow field within the chip, thereby enhancing the contact frequency between cells and aptamers and ultimately improving the capture rate. The proposed chip demonstrated a capture efficiency of approximately 91.87% for human breast cancer cells (MCF7), with a release rate of 77.5%. The relative activity of the released cells was approximately 94.08%. Notably, the specificity of the aptamers toward tumor cell surface antigens enables high-purity capture. Additionally, the use of DNA enzymes to digest aptamers facilitates the release of high-activity CTCs, offering a method to simultaneously achieve a high capture rate, purity, and activity enrichment.

Key words: Circulating tumor cell (CTC); Cell sorting; Microfluidic chip; Two-photon polymerization; Deterministic lateral displacement

1 Introduction

Cancer is a leading threat to human longevity (Sung et al., 2021). In patients with cancer, some tumor cells become detached from the primary tumor, enter the circulatory system, and then travel throughout the body, where they may infiltrate normal tissues to colonize and form new tumors. This process is known as cancer metastasis. Cancer metastasis includes four processes: local invasion, infiltration, exosmosis, and colonization, which is responsible for up to 90% of cancer deaths (Chaffer and Weinberg, 2011; Li et al., 2024). Detached tumor cells are also called circulating tumor cells (CTCs) (Alix-Panabières and Pantel, 2014; Shu et al., 2024). Enrichment and detection of CTCs in peripheral blood is of great significance for early tumor diagnosis, prognosis and risk assessment of metastasis and recurrence (Cristofanilli et al., 2004; Cohen et al., 2006; de Bono et al., 2008), efficacy

✉ Liang MA, liangma@zju.edu.cn
Xiaobin XU, xiaobinxu@tongji.edu.cn
* The two authors contributed equally to this work
Liang MA, https://orcid.org/0000-0002-6242-1850

Received Aug. 8, 2025; Revision accepted Nov. 3, 2025; Crosschecked Mar. 10, 2026; Online first Apr. 1, 2026

evaluation and medication guidance regarding tumor precision therapy (Cortés-Hernández et al., 2020; Liu et al., 2023), and monitoring of dynamic markers during tumor therapy (Smerage et al., 2014; Ma and Yang, 2023).

The scarcity and heterogeneity of CTCs present substantial challenges to the enrichment, isolation, and subsequent detection of CTCs from blood samples. Existing CTC capture techniques can be roughly divided into two categories: physics-based capture and immune-binding capture (Kang et al., 2022; Liu et al., 2022; Hu et al., 2025).

Physics-based capture is mainly based on the differences in certain physical properties (such as size, density, deformations, and dielectric properties) of CTCs and blood cells. It includes methods such as centrifugal separation (Rosenberg et al., 2002; Low and Abas, 2015), filtration separation (Sarioglu et al., 2015; Kang et al., 2017; Zhang et al., 2018; Chen et al., 2024), fluid mechanical separation (Zeming et al., 2013; Park et al., 2016; Renier et al., 2017; Salafi et al., 2019; Xiang et al., 2019), dielectrophoresis separation (Varmazyari et al., 2022; Wu et al., 2023), and acoustic electrophoresis separation (Antfolk et al., 2017; Wu et al., 2018). For instance, Rosenberg et al. (2002) showed that both the OnceQuick and Ficoll systems achieved a capture efficiency of 70%–90% when separating rectal cancer HT-29 cells from blood. Moreover, Kang et al. (2017) captured nine different types of cancer cells using filters with conical slits, with an average capture rate of 77.7%; a vitality of 80.6% was also maintained for the cells. However, such physical capture methods generally possess the shortcomings of a low capture rate, low capture purity, and low cell activity following capture.

The immune binding method uses certain molecules (antibodies or aptamers) to bind specifically to the surface antigens of cancer cells to capture CTCs (Sheng et al., 2013; Galletti et al., 2014; Zhou and Rossi, 2017; Shi et al., 2022; Kang et al., 2025). Considering the differences in the grafted surfaces of antibodies or aptamers, this method can be roughly divided into two categories: immunomagnetic separation and functionalized micro/nanostructure separation. Yu et al. (2013) affixed antibody-modified iron (III) oxide nanoparticles on nickel microcolumns using a magnetic field to fabricate a CTC capture chip, which can separate CTCs by simply removing the magnetic field. Additionally, Zhang et al. (2012) functionalized antibodies against horizontally stacked electrospun titanium dioxide nanofibers for the capture of CTCs and increased the capture rate by utilizing the interaction between the substrate and the extracellular matrix surface. CTC capture techniques based on immune binding tend to require a longer incubation period to induce cell binding to antibodies or aptamers, resulting in lower fluxes. Meanwhile, some antibody-based capture methods can release tumor cells through proteolytic hydrolysis of antibodies, which will affect the activity of tumor cells and the number of membrane proteins; this complicates subsequent analysis of tumor cells.

To overcome the limitations of existing CTC capture technologies—namely, low capture rate, low purity, and insufficient activity of the captured CTCs—a microfluidic chip based on the immune binding principle that leverages a herringbone-shaped microchannel and deterministic lateral displacement technology was proposed. Using the advanced two-photon-polymerization fabrication method, the bottom capture unit can be fabricated with high resolution with high reproducibility. Moreover, by influencing the flow field inside the chip (Lin et al., 2023), the contact frequency between cells and aptamers can be increased, and the capture rate can be improved. The specificity of aptamers to tumor cell surface antigens is used to achieve high purity capture. The digestion of aptamers by deoxyribonuclease (DNase) is also leveraged to promote high activity release of the captured CTCs.

2 Materials and methods

The content of this paper mainly consists of three parts: first, structural design of the top herringbone-shaped microchannel and the bottom column is performed, then the designed chip is processed and the aptamer is modified, and finally, the capture experiment is conducted to verify the effectiveness of the simulation and explore the optimal operational parameters of the chip. Following this research content, the overall framework is illustrated in Fig. 1.

2.1 Materials

An SU-8-3050 photoresist was purchased from MicroChem (USA). Polydimethylsiloxane was obtained

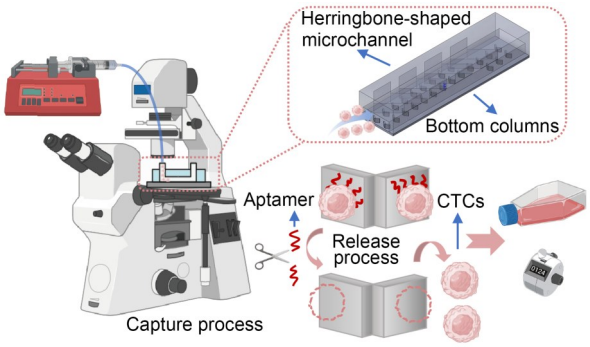

Fig. 1 Schematic of the CTC capture system

from Dow Corning (USA). An IP-Dip2 photoresist was supplied by NanoScribe (Germany). Cell Tracker Red CMTPX and Cell Tracker Green CMFDA were purchased from Thermo Fisher (USA). (3-Mercaptopropyl) trimethoxysilane (MPTS), propylene glycol monomethyl ether acetate (PGMEA), and 4-maleimidobutyric acid N-hydroxysuccinimide ester (GMBS) were purchased from Aladdin (China). Streptavidin, Alexa Fluor 680-labeled streptavidin, DAPI solution, Tween-20, bovine serum albumin (BSA), and red blood cell lysis buffer were obtained from Solarbio (China). The human breast cancer cell line MCF-7 and the human chronic myeloid leukemia cell line K562 (both with complete media) were purchased from Saibaikang (China). FITC-labeled phalloidin was supplied by Yisheng (China). Recombinant DNase I, mouse-derived recombinant EpCAM antibody, and Cy5-labeled goat anti-mouse IgG were purchased from Saivier (China). The biotinylated SYL3C aptamer and Cy5-labeled aptamer were synthesized by Tsingke Biotechnology Co., Ltd. (China).

2.2 Chip fabrication

The top structure of the chip was constructed using soft lithography technology, which is common for microfluidic devices. In short, the SU-8 mold was first engraved, and then the top herringbone-shaped microchannel was constructed using polydimethylsiloxane (PDMS) reverse molding and drilling. The bottom structure was established through a two-photon polymerization (TPP) method using a 3D TPP printer (PPGT2, Nanoscribe, Germany) with its 3D SF Dill module (63-fold objective) and IP-Dip2 photoresist. The 3D model was built using SolidWorks and sliced using Describe software (version 2.7) after completion, and the output GWL file was imported into Nanowrite software (version 1.10.5) for printing. The microstructure is then printed on silylated fused quartz glass with a glass size of 75 mm×25 mm×1 mm. The quartz glass with the top PDMS and the bottom printed with the microstructure was treated with oxygen plasma at 50 W for 30 s, and subsequently, the assembly was completed through alignment and pressing under an industrial microscope.

2.3 Aptamer modification

The aptamer modification process was performed following the manufacturer's instructions. To summarize, an anhydrous ethanol solution of 5% (volume fraction) MPTS was injected into the chip and incubated at room temperature for 30 min to graft the sulfhydryl groups. After rinsing with anhydrous ethanol, 10 mmol/L GMBS anhydrous ethanol solution was injected and incubated at room temperature for 30 min to graft the N-Hydroxysuccinimide (NHS) ester. Following this rinsing, 50 μg/mL streptavidin was injected and incubated overnight. Finally, the modification was completed after rinsing with phosphate-buffered saline (PBS) and injecting 1.5 μmol/L biotinylated aptamer with a 2 h incubation time.

2.4 Tumor cell culture

The tumor cell lines were cultured in the corresponding complete medium in a 37 °C incubator with 5% carbon dioxide. The EpCAM-positive human breast cancer cell line MCF-7 was used as the model CTC, and the EpCAM-negative human chronic myeloid leukemia cell line K562 was used as the model leukocyte.

2.5 Cell capture and release

Before the capture experiment, live cells were stained with 1 μmol/L Cell Tracker Red CMTPX or Cell Tracker Green CMFDA to facilitate follow-up observations and counting. To prepare the cell suspension for capture, MCF-7 was first digested with pancreatic enzyme-free cell digestion solution, the supernatant was discarded after centrifugation, and then resuspension was performed with phenol-free red Dulbecco's modified eagle medium (DMEM). For suspension K562 cells, the digestion step can be omitted. The cells were counted using a hemocytometer, and specific cell concentrations of MCF-7 and K562 single cells or mixed cell suspensions were prepared

using gradient dilution. The suspension was then extracted into a 1 mL syringe and injected into the microfluidic chip with an injection pump at a constant flow rate. Subsequently, 500 μL of PBS buffer was injected to flush out the uncaptured cells, and subsequent counting and other operations were performed.

After the capture and flushing process, the captured cells were counted under an inverted fluorescence microscope. Considering the number of captured cells for N_1 and the total number of cells N, the capture rate R_c can be calculated as:

$$R_c = \frac{N_1}{N} \times 100\%. \tag{1}$$

Cell release was performed using Recombinant DNase I by first combining Recombinant DNase I, dilutive solution, and ultrapure water in 1 U:1 μL:10 μL. Then, the working liquid was injected into the chip and incubated at 37 ℃ in the incubator for half an hour. Thereafter, 2 mL of phenol-free red DMEM was injected into the chip to flush out the released cells. The cells that were not released were counted under an inverted fluorescence microscope. With the number of cells that are not released being N_2, the release rate R_r can be calculated as:

$$R_r = \frac{N_1 - N_2}{N_1} \times 100\%. \tag{2}$$

2.6 Statistical analysis

All data are presented as the mean±standard deviation (SD) values from at least three independent experiments. The significant difference between the control group and the experimental group was assessed using the independent samples *t*-test. All analyses and plotting were performed using Origin (Version 2024, OriginLab Co., USA). A *P*-value less than 0.05 was considered statistically significant.

3 Results and discussion

3.1 Chip top structural design

The top structure of the CTC capture chip was constructed as a herringbone-shaped microchannel. The herringbone-shaped mixer is simple and easy to manufacture and is commonly used in microfluidics. Micro-vortexes can be generated in the microchannel, promote the diffusion of the fluid through the stretching and folding of the fluid volume, and achieve mixing of various fluids. Applying the herringbone-shaped mixer in the capture of CTCs can increase the frequency of cell collisions with the wall and thus increase the capture rate.

The basic size of the herringbone-shaped microchannel structure is shown in Fig. 2a. The dimensions of the microchannel are described by the minimum element width ω, asymmetry p, runner height h, height αh, width ω_1, spacing d, and deflection angles α_1 and α_2.

The size parameters of the herringbone mixer were set according to existing studies. For instance, Stroock's research showed that when $\alpha_1=\alpha_2=45°$ and $\frac{2\pi\alpha h}{\omega_1 + d} \sim 2$, the herringbone mixer showed the greatest transverse flow (that is, the ratio of transverse to axial flow) (Stroock et al., 2002). Therefore, we take $\alpha_1 = \alpha_2 = 45°$ and $\frac{2\pi\alpha h}{\omega_1 + d} \sim 2$. Moreover, a simulation study of Li and Chen (2005) showed that a herringbone asymmetry of 0.6 displayed the greatest transverse flow. Thus, we set the asymmetry degree of the herringbone-shaped microchannel to 0.6.

High susceptibility to clogging is a common problem in microfluidic chips used for CTC capture. To address this, we must design the flow path height to accommodate the size of the CTCs. CTCs are 15–40 μm in diameter, and thus, the flow channel height needs to be above 40 μm. However, for the sake of more accurate control of the fluid and cell movement in the channel, the flow height should not be too large. Therefore, the flow channel height is set at 50 μm. The preliminary design of the herringbone-shaped microchannel is summarized in Table 1, and simulation design is only needed for ω, ω_1, and d. The purpose of the top herringbone design is to promote frequent contact between the fluid and the cells within the fluid and the wall. Accordingly, the target physical quantity was the average flow velocity v_{yz} perpendicular to the mainstream directional plane, which is the volume fraction of v_{yz}.

First, the herringbone spacing d was designed. The size ranges needed to be delineated at an early stage of the design process. If the herringbone shape spacing is too small, it will cause difficulties in fabrication, so the minimum value of the spacing was set

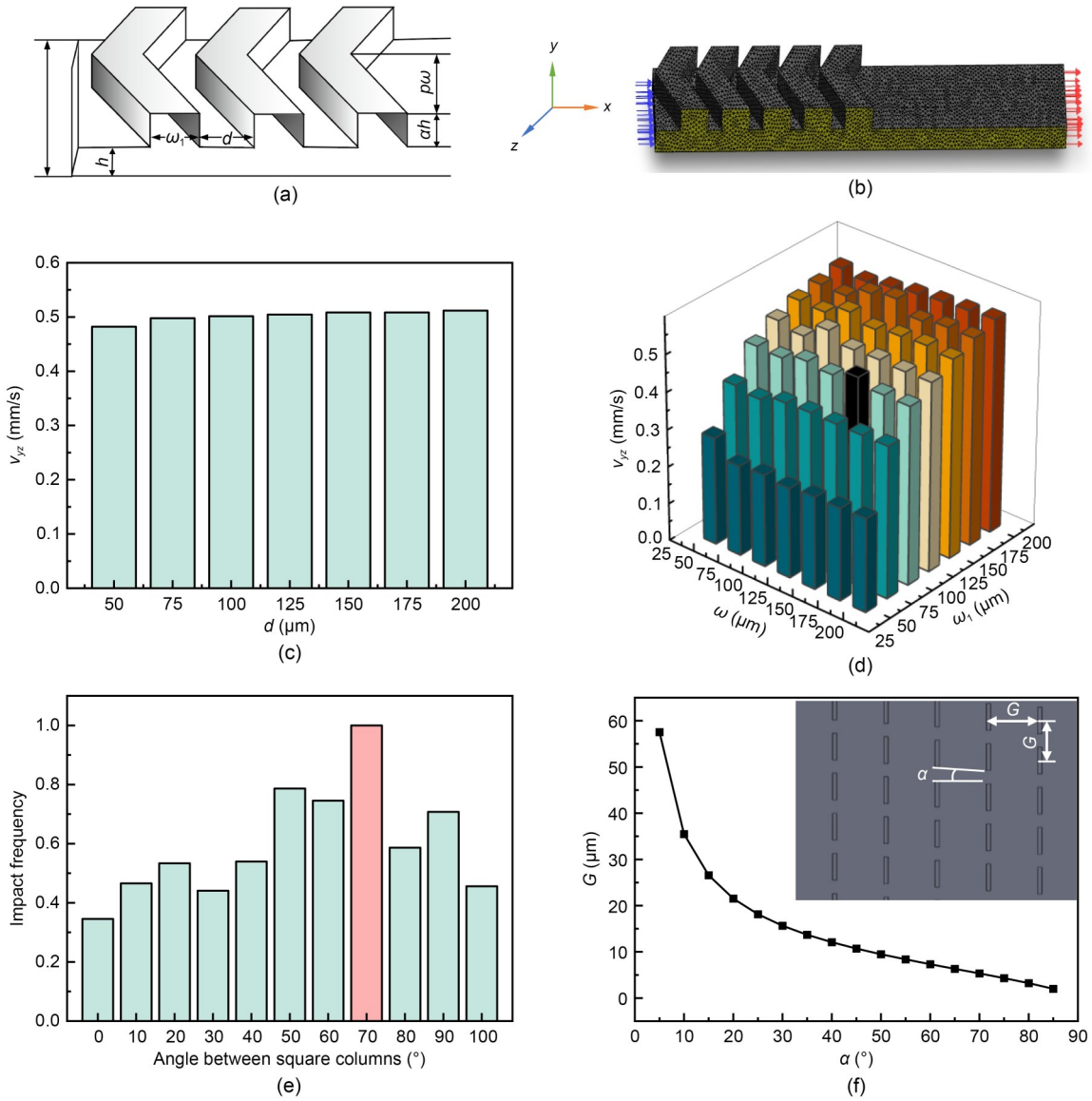

Fig. 2 Chip structure design and optimization: (a) diagram of the basic dimensions of the herringbone-shaped structure; (b) mesh diagram; (c) relationship between v_{yz} and the herringbone shape spacing d; (d) relationship between v_{yz} and the herringbone shape width and minimum element width; (e) relationship between the angle of the square column and the collision frequency (normalized); (f) schematic diagram of the column parameters and the relationship between spacing G and offset angle α

as 50 μm, the maximum was 200 μm, and the gradient was 25 μm. The minimum element width of the fixed herringbone shape is 150 μm, and the herringbone shape width is 100 μm. The simulations of the relationship of v_{yz} with d are shown in Fig. 2c. It can be observed that with the increase of d, the change in v_{yz} is very small; thus, to increase the number of vortices, the number of herringbone grooves should be increased. Hence, the herringbone spacing was set at a smaller value of 50 μm.

After determining the herringbone spacing d, there are only two remaining parameters, ω and ω_1, to be optimized. First, we need to determine their size limits to constrain the simulation optimization. If the minimum element width ω is too small, it will increase the aspect ratio of the structure, which is not conducive to development and engraving. Therefore, the minimum for the size range of ω is determined to be 50 μm—consistent with the height of the flow channel. If ω is too large, the total number of vortices will

Table 1 Preliminary restrictions on the basic dimensions of the herringbone shape

Parameter	Dimension	Basis of determination
α_1	45°	Stroock et al. (2002)
α_2	45°	Stroock et al. (2002)
α	$\frac{2\pi\alpha h}{\omega_1+d}\sim 2$	Stroock et al. (2002)
ω_1		
p	0.6	Li and Chen (2005)
h	50 μm	Determined by the size of the CTCs and their movement within the fluid
d	Undetermined	
ω	Undetermined	

be slightly reduced, so the maximum size was set as 200 μm and the gradient was set as 25 μm. The size range and gradient of the herringbone width ω_1 are the same as for the minimum element width ω. Using the size range and gradient of the two models, 49 flow-domain models were established. The relationship between the simulated v_{yz} and the minimum cell width ω and herringbone width ω_1 is shown in the 3D bar chart in Fig. 2d.

Fig. S1a of the electronic supplementary materials (ESM) shows that when the minimum element width ω is fixed, with increasing herringbone width ω_1, the average flow velocity perpendicular to the main flow plane increases rapidly at first and then slows. Looking at the vector diagram of v_{yz} corresponding to different herringbone widths ω_1 in Fig. S2 of the ESM, one can see that the larger values of v_{yz} only appear where the fluid enters and exits the herringbone. This is because when the fluid flows to the onset of the herringbone shape, it will flow upward and fill the herringbone-shaped groove; then, when it flows to the end of the herringbone, it will flow downward and exit the groove. Therefore, the v_{yz} value at the beginning and end of the herringbone channel is larger, while the velocity component perpendicular to the main flow direction is smaller for flow in the groove. When the width of the herringbone ω_1 is larger, the v_{yz} value in the middle of the herringbone channel is smaller. It is clear that if the width ω_1 of the herringbone channel is too large, the number of vortices per unit length will be reduced. Therefore, the herringbone channel's optimal width is 100 μm.

At the same time, Fig. S1b shows that there is no obvious correlation between v_{yz} and the minimum element width ω when the herringbone width ω_1 is fixed. To facilitate fabrication, we must ensure the aspect ratio of the structure, so the minimum unit width is set to be 3 times the height of the flow channel, that is, 150 μm.

3.2 Chip bottom structural design

The deterministic lateral displacement (DLD) principle refers to how when particles with different sizes flow through a microcolumn array, particles with a diameter larger than the critical diameter frequently collide with the column, and particles with a diameter smaller than the critical diameter follow the flow path. At present, this principle has been widely used to separate blood cells (Catarino et al., 2019), extracellular vesicles (Santana et al., 2014; Havers et al., 2023), submicron particles (Zhang et al., 2020), and nanoparticles (Xie et al., 2020). The application of this method in CTC capture can cause cells to collide with the bottom structure more frequently, thus increasing the probability of capture. Accordingly, a deterministic transverse displacement column was selected as the bottom structure of the CTC capture chip in this study.

The design of the top herringbone-shaped microchannel causes the fluid to flow in a spiral pattern in the flow channel, and thus, the design of the bottom structure should make the surface of the microcolumn as perpendicular as possible to the velocity direction of the cells. Therefore, we opt to design the bottom microcolumn as a square column with a certain angle. A high blockage tendency is a common problem in CTC capture based on the DLD principle. To reduce the probability of blockage, a column height of 20 μm was selected. Moreover, to simplify the design process, the column length was also set to 20 μm.

Currently, relevant studies on columns leveraging the DLD principle are relatively mature, and there is an empirical design formula for square columns (Zhang et al., 2015) as follows:

$$D_c = 1.4G\xi^{0.69}, \tag{3}$$

where D_c is the critical diameter, G is the column spacing, and ξ is the tangent value of the offset angle. According to this formula, the spacing and deviation angle of the column array will affect the frequency of collisions between the particles and the bottom structure, so the spacing and deviation angle of the column array must be designed first. Since the average diameter of the human breast cancer cell line MCF-7 used

in subsequent experiments was 15 μm, the critical diameter was taken as this value. When the critical diameter is 15 μm, the relationship between the column spacing and deviation angle is shown in Fig. 2f. To prevent blockage, the maximum spacing was set to 60 μm, and the corresponding offset angle was 5°. The column shape is designed below, and the angle θ of the square column is designed first. The included angle range is 0°–100°, and the included angle gradient is 10°. The higher the collision frequency between CTCs and the bottom structure, the greater the probability of CTC capture. Therefore, the simulation design of the bottom structure was based on a selected collision frequency between the particles and the bottom structure, that is, the ratio of the number of collisions between the particles and the bottom structure to the total number of particles. The relationship between the simulated column angle and the normalized collision frequency is shown in Fig. 2e. It can be seen that with the increase in the square column angle, the collision frequency first increases and then decreases, so accordingly, we take the angle of the square column as 70°.

For further design of the column shape, we considered changing the simple square column into a more complex 3D structure. However, when meshing complex columns, very fine grids are needed to reflect the bottom structure more accurately, which makes calculations difficult. Thus, further design of the columns is instead informed by subsequent experiments.

3.3 Chip fabrication

Scanning electron microscope (SEM) and light microscope images of the PDMS after mold inversion are shown in Figs. 3a and 3b, respectively. In Fig. 3a, PDMS was placed on the 30° stage and sprayed with gold. The actual flow path height was twice the measured length, that is, 50 μm. Clearly, the microchannel size is basically consistent with the design size. At the same time, the mold remains intact after over 10 cycles of mold reversal, and thus, it can be seen that the aspect ratio of the structure is effective. The smaller aspect ratio enables the micro-convex portion of the mold to suffer less shear force during the mold reversal, making it more difficult for the microstructure to fall off.

The bottom structure was processed with two-photon polymerization, with the bottom microstructure revealed through SEM in Fig. 3c. The complete assembled microfluidic chip and the system for CTC capture are shown in Fig. 3d.

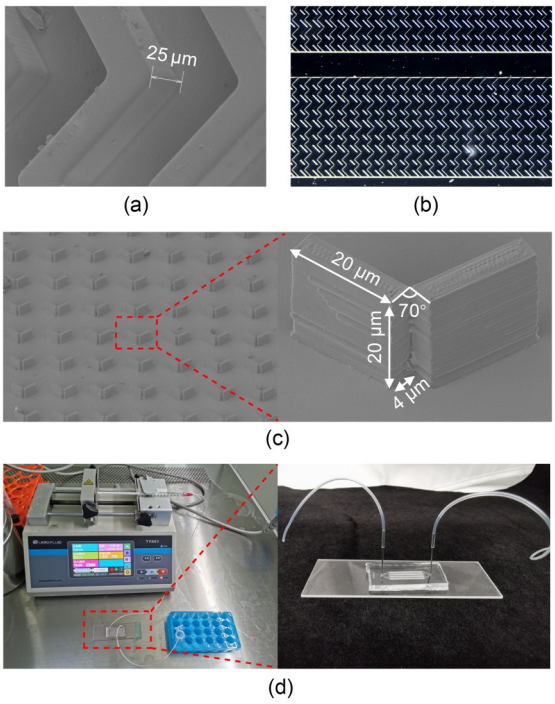

Fig. 3 Schematic diagram of the bottom and top of the chip: (a) SEM image of the top structure of PDMS after mold inversion; (b) optical microscope image of the top structure after mold inversion; (c) SEM diagram of the bottom structure; (d) operation of the CTC capture system

3.4 Chip performance characterization

The performance of the chip can mainly be described by the capture rate, release rate, cell activity after release, and capture purity. The relationship between the flow rate and capture rate was explored to determine the optimal flow rate for capture. As shown in Fig. 4a, with increasing flow velocity, the capture rate generally decreases. To maximize the processing flux of the chip and ensure an adequate capture rate of CTCs, the flow rate for subsequent capture experiments was selected as 1 mL/h.

To verify the effectiveness of the design of the bottom structure, bottom columns with angles of 0°, 70°, and 140° were printed, and the herringbone-shaped microchannel designed in the previous section was used for three sets of capture experiments on the top of the three columns. The statistical capture rate is shown in Fig. 4b. When the angle of the square column was 0°, the capture rate was approximately 75.37%;

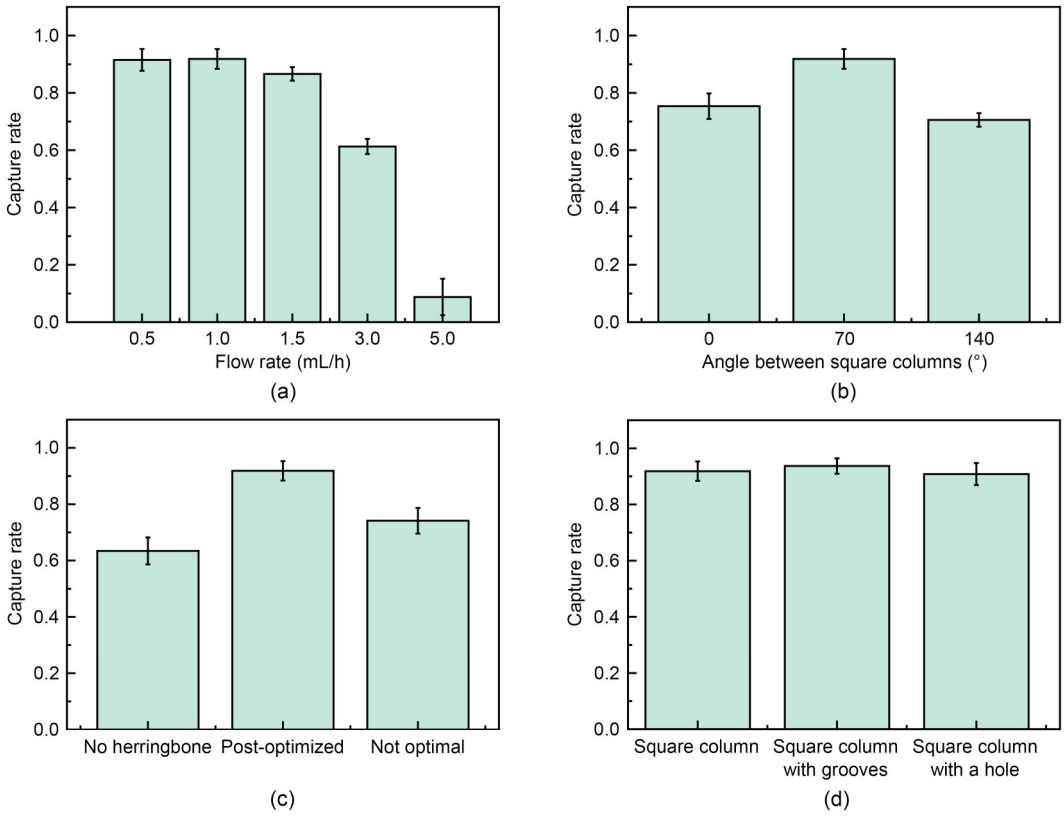

Fig. 4 (a) Relationship between flow rate and capture rate; (b) relationship between the angle of the square column and the capture rate; (c) capture rate corresponding to the chip with different top structures; (d) capture rate of the chip with different square column shapes at the bottom. All the above results are expressed as the mean±SD from three independent experiments

when the angle of the square column was 70°, the capture rate was approximately 91.87%; when the angle of the square column was 140°, the capture rate was approximately 70.57%. As the angle of the square column increases, the capture rate first increases and then decreases, which is consistent with the simulation results. To verify the effectiveness of the top structure design, three groups of top structures were tested: one without a herringbone-shaped microchannel, one with a herringbone-shaped microchannel after simulation optimization, and one with a non-optimal herringbone-shaped microchannel with a minimum element width of 150 μm and herringbone shape width of 50 μm. The bottom structures of the three groups were all 70° angle square columns following optimization. The capture rates of the three groups are shown in Fig. 4c. The capture rate of MCF-7 is approximately 63.43% for the microfluidic chip using the top flow channel without a herringbone shape and 74.13% for the microfluidic chip using the top flow channel with a minimum cell width of 150 μm and a herringbone shape width of 50 μm—these results are also consistent with the simulations.

Next, two more complex 3D columns were printed for capture, and the influence of column shape on the capture rate was explored. To increase the effective area of the aptamer modification, four slots that were 2 μm wide, 20 μm long, and 2.5 μm deep were etched into the surface of the square column for the first type of column shape, as shown in Fig. S3a of the ESM. The second type of column makes a ball-shaped groove on the surface of the square column, as depicted in Fig. S3b. The chip was assembled using the optimized top herringbone-shaped microchannel and the bottom structure composed of two derived cylindrical arrays, and the capture experiment was conducted on MCF7 cell suspension with a cell density of 1×10^3 mL^{-1}, with the results shown in Fig. 4d. The capture rate of CTCs for the chip with the grooved square column at its bottom was approximately 93.70%, for the chip with the spherical hole square column it was approximately 90.80%, and for the chip with the simple square

column it was approximately 91.87%. Therefore, these more complex 3D columns did not have a significant effect on the capture rate.

The release of the trapped cells was then investigated. First, the DNase treatment time and aptamer degradation rate were investigated using Cy5-labeled aptamers to determine the optimal DNase treatment time for cell release. A 100 μm×100 μm×10 μm square array was printed and treated with DNase for 5, 10, 15, and 20 min after modification; the fluorescence intensity was then measured. As shown in Fig. 5c, with increasing DNA enzyme treatment time, the release efficiency of the aptamer gradually increased, with the release rate reaching approximately 75.0% after an incubation time of 15 min, and then the increasing trend slowed as the incubation time increased further. To minimize the incubation time of cells in the DNase without nutrients, the subsequent DNase incubation time was set at 20 min. After the incubation, the captured MCF7 was released.

The fluorescence images before and after release are presented in Fig. 5d. Statistically, the release rate was approximately 77.57%. The release rate to cells was slightly lower than that to aptamers. Theoretically, a single cell needs multiple pairs of antigens to bind to the aptamer to fix to the wall, so the release rate of DNase to the cell should be greater than that of the aptamer; however, the experimental results are contrary to this. The reasons for this may be as follows: First, a small number of cells adhere to the wall nonspecifically; that is, they are not fixed on the wall by binding with the aptamer, so the aptamers decomposed through DNA enzymes cannot be released. Second, DNA enzymes may not fully degrade the aptamer into deoxyribonucleotides but only degrade long aptamer chains into several short chains and thus not completely separate the aptamer from the wall. For the fluorescent aptamer used in the DNase release experiment, the fluorophores are modified at its ends, and the degradation of any single chain can cause the fluorophores to break

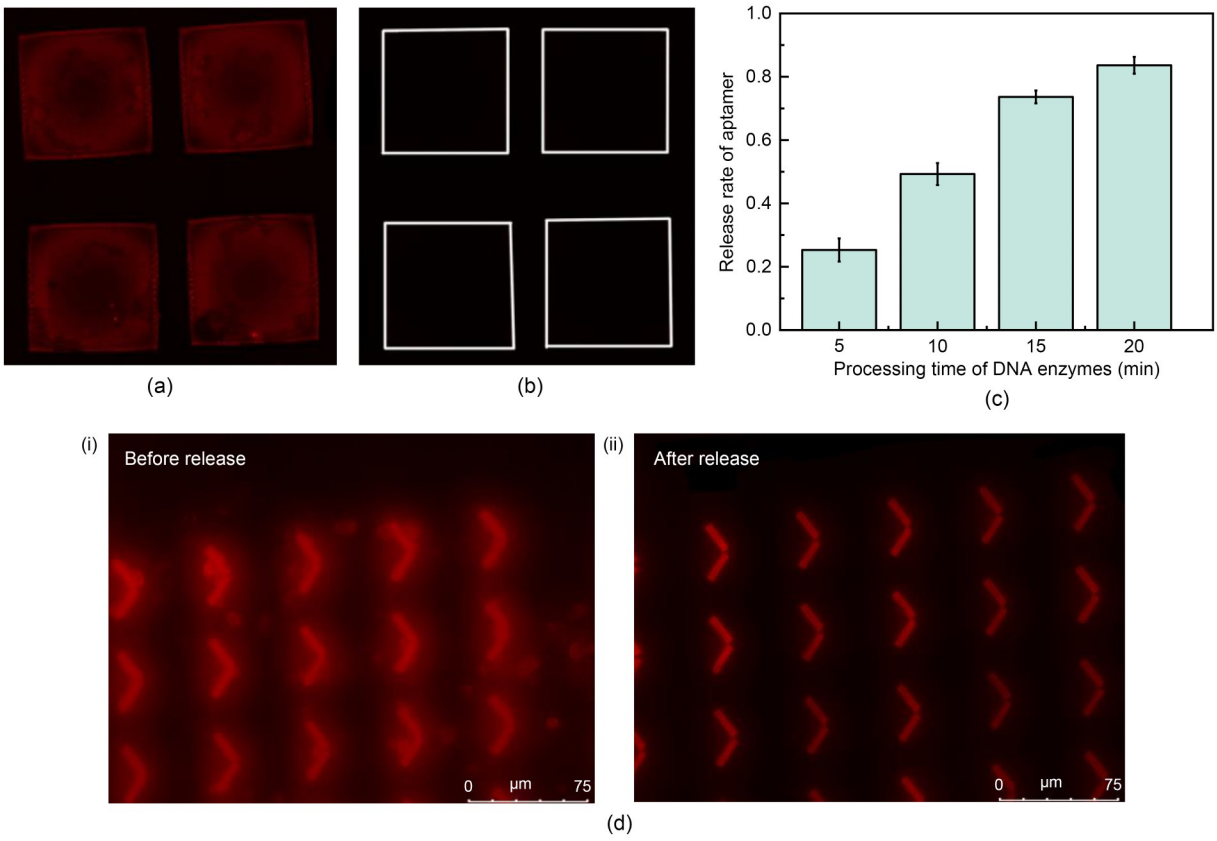

Fig. 5 DNA enzyme release effect and statistical diagram of the aptamer: (a) fluorescence pattern of the anterior block treated by DNase; (b) surface fluorescence of the block after 20 min of DNase treatment; (c) relationship between DNase treatment time and aptamer release rate, where the results are expressed as the mean±SD from three independent experiments; (d) fluorescence images of captured cells before and after release

away from the wall and cause the wall to lose its red fluorescence, thus leading to the difference between the two groups of experiments.

Subsequently, the cell activity after release was investigated. During the process of capture and release, cell activity is affected by the following factors: digestion using pancreatin-free cellular digestive fluid, the shear process during capture, and the release of captured cells using DNA enzymes. Therefore, live/dead staining was performed on the cells after the three processes, and the results are presented in Figs. 6a and 6b. The cell activity after digestion by pancreatin-free cell digestive fluid was approximately 77.47%, and the cell activity after capture and release was approximately 72.88%; therefore, the relative activity of cells after capture and release was 94.08%. Moreover, it is clear that the 1 mL/h flow rate and the DNA enzymes had no significant effect on cell activity. After this experiment, the released cells were recultured, with the results demonstrating that the released

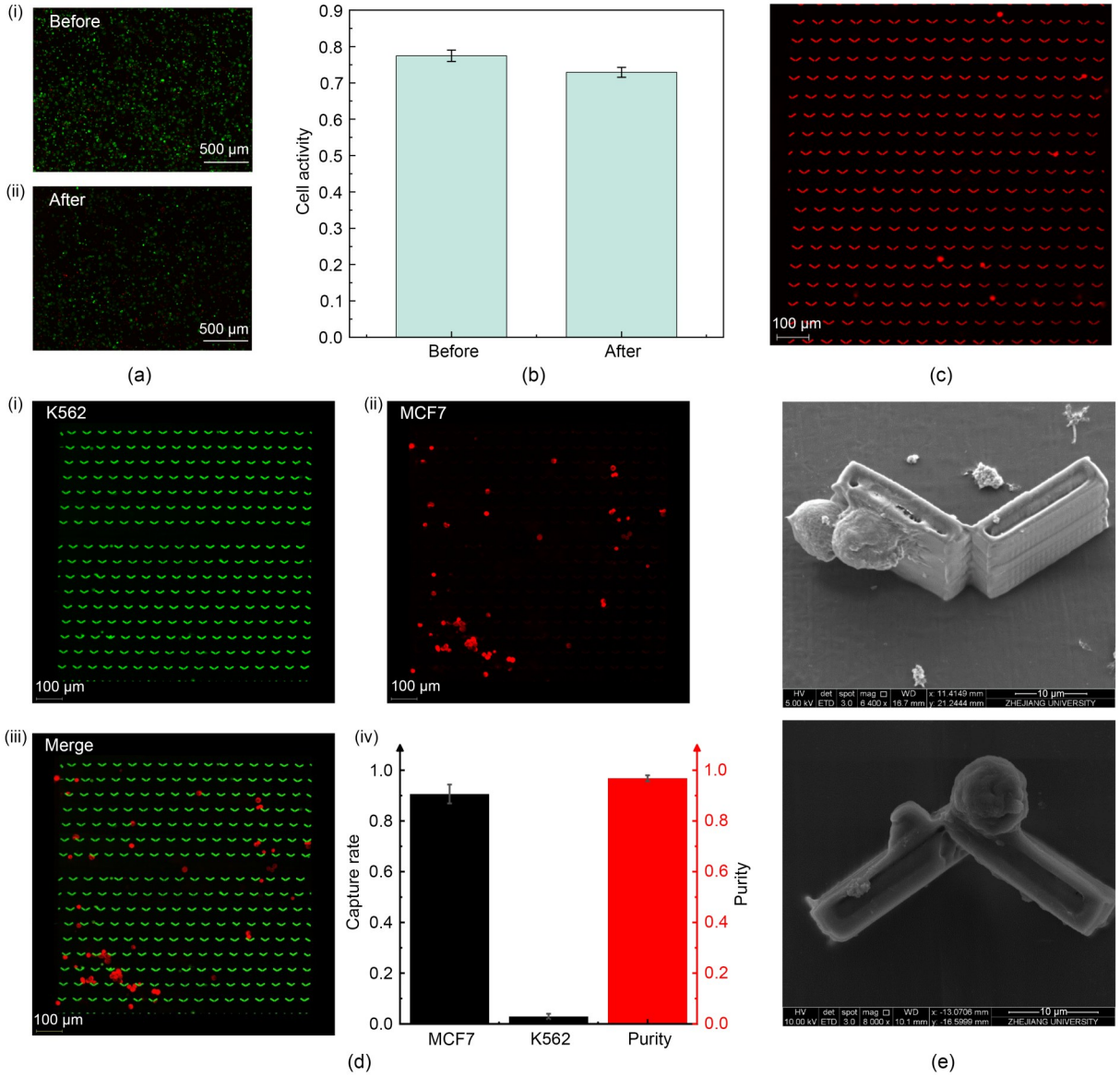

Fig. 6 (a) Live/dead staining images of precaptured cells (a-i) and the cells after capture and release (a-ii), where red represents dead cells, and green represents live cells; (b) statistical graphs of cell activity before and after capture and release; (c) fluorescence images of EpCAM-negative cells captured by the chip; (d) fluorescence images and statistical data of two kinds of cells captured by the bottom structure in the mixed cell suspension; (e) SEM images of the cells captured by the bottom structure. The results of (b) and (d) are expressed as mean±SD from three independent experiments

cells were able to proliferate normally in the culture bottle.

Subsequently, approximately 1000 mL^{-1} Cell Tracker red-labeled EpCAM-negative K562 cells were used for capture experiments, with the captured cells shown in Fig. 6c. According to the resulting statistics, the capture rate of K562 cells was 4.83%. Then, approximately 1000 mL^{-1} EpCAM-positive MCF7 cells and approximately 1000 mL^{-1} EpCAM-negative K562 cells were mixed at a ratio of 1:1 for capture. The fluorescence diagram of captured cells after rinsing is shown in Fig. 6d. The captured MCF7 cells were observed with SEM at 45° and from a top view (Fig. 6e). The capture rate of the two kinds of cells was statistically measured. The capture rate for EpCAM-positive MCF7 cells was approximately 90.63%, the capture rate for EpCAM-negative cells was approximately 2.93%, and the capture purity was approximately 96.83%. Compared with the capture of a single cell, the capture rate of both cell types decreased in the mixed cell suspension. The data show that the capture rate of positive MCF7 cells by the chip dropped from 91.87% to 90.63%. There may be two reasons for this decline in the capture rate of MCF7: First, K562, which experiences nonspecific adhesion to the wall, occupies a position where MCF7 may be bound to the aptamer. Second, there is a collision between MCF7 and K562, which will affect the original movement of MCF7. Both of these factors will lead to a decrease in the contact frequency between MCF7 and the aptamer, thereby resulting in a lower capture rate. The reason for the lower capture rate of K562 may be that the aptamer-bound MCF7 occupies the non-specific binding position of K562. These results demonstrate that the proposed chip can be used for effective CTC capture with excellent sensitivity in complex cell mixture conditions; our methodology therefore shows promise for real blood flow scenarios with red and white blood cells.

To better position the advancement of this work, the performance of our system is briefly compared with that of several state-of-the-art systems. For instance, our platform achieved a capture rate of 91.87%, which compares favorably with the 86.37% reported by Wu et al. (2023)—they used a dielectrophoresis-based method involving inkjet printing of microelectrode arrays onto thin films. The advantages of our method are particularly evident in terms of purity and release rate. For instance, compared with the functionalized nano-magic-clip capture chip based on the immune binding principle by Sun et al. (2022), at a similar capture rate (89.9%), we achieved a capture purity of 96.83% and a release rate of 77.57% under mixed cell conditions. This is crucial for the effectiveness of CTC detection, which has rarely been explored in previous studies.

Additionally, maintaining the cell survival rate after separation is an important issue that has not been fully addressed in earlier research. The relative activity of the cells released by our method is approximately 94.08%, while existing capture methods with high capture rates based on dielectrophoresis principles often bring along issues such as a relatively high electric field intensity in the microchannels and the Joule heating effect; these can cause irreversible damage to the cells and thereby affect the activity of the released cells. We primarily attribute the comprehensive performance enhancement shown in our study to the integration of the principle of immunoaffinity and deterministic lateral displacement technology. This design achieves a balance between the capture and release mechanisms, avoiding trade-offs between high purity, efficient release, and cell activity. Therefore, this comparison underscores that our methodology presents a balanced and effective solution and pushes the limits of multiple key performance metrics.

However, to apply this technology in future clinical practice, it is imperative to improve upon discrete and labor-intensive manual operation procedures. Therefore, a critical direction for our future work will be the development of a semi- or fully-automated, integrated platform that combines the steps of sample introduction, capture, purification, release, and subsequent analysis. This would significantly reduce operator-induced variability, improve reproducibility, shorten the time needed for analysis, and thereby facilitate potential liquid biopsy applications in clinical settings.

4 Conclusions

A novel CTC capture chip was designed through computational fluid dynamics simulations of structures with herringbone-shaped mixers and deterministic lateral displacement technology. Soft lithography

and two-photon polymerization technology were used to complete the processing of the chip, and an aptamer was grafted inside the chip for specific capture of CTCs. The capture rate of the human breast cancer cell line MCF7 was approximately 91.87%, the release rate was approximately 77.57%, and the relative activity of the cells after release was approximately 94.08%. The capture rate of the negative human chronic myeloid leukemia cell line K562 was approximately 4.83%, and the capture purity of positive cells in the presence of mixed cells was approximately 96.83%. Our results demonstrated that the proposed CTC capture chip can achieve a high capture rate, high purity, and high activity enrichment of CTCs, thus providing an effective platform for CTC detection and diagnosis. With future advancements in integration and automated development, this method may be impactful in clinical practice.

Acknowledgments

This work is supported by the State Key Laboratory of High-performance Precision Manufacturing (No. HPMKF202412), the Zhejiang Provincial Natural Science Foundation of China (No. LZ25E050001), the National Natural Science Foundation of China (No. 52275294), and the Zhejiang Provincial 'Pioneer Leading Swan+X' Science and Technology Program (No. 2025C02122), China.

Author contributions

Xinyi LIANG and Changwei QIN performed most of the experiments and wrote the manuscript. Kaiqiang LI, An REN, Jiarui HU, Weikang LV, and Lunan KE performed some of the experiments and helped with the data analysis. Mengfei YU, Zhen WANG, and Xiuxiu JIANG discussed and edited the manuscript. Huayong YANG provided the resources. Xiaobin XU and Liang MA supervised the manuscript process and revised and edited the manuscript.

Conflict of interest

Huayong YANG is an Editor-in-Chief of this journal, and is NOT involved in the editorial review or the decision to publish this article. Xinyi LIANG, Changwei QIN, Kaiqiang LI, An REN, Jiarui HU, Weikang LV, Lunan KE, Zhen WANG, Mengfei YU, Xiuxiu JIANG, Huayong YANG, Xiaobin XU, and Liang MA declare no conflict of interest.

References

Alix-Panabières C, Pantel K, 2014. Challenges in circulating tumour cell research. *Nature Reviews Cancer*, 14(9):623-631.
https://doi.org/10.1038/nrc3820

Antfolk M, Kim SH, Koizumi S, et al., 2017. Label-free single-cell separation and imaging of cancer cells using an integrated microfluidic system. *Scientific Reports*, 7(1):46507.
https://doi.org/10.1038/srep46507

Catarino SO, Rodrigues RO, Pinho D, et al., 2019. Blood cells separation and sorting techniques of passive microfluidic devices: from fabrication to applications. *Micromachines*, 10(9):593.
https://doi.org/10.3390/mi10090593

Chaffer CL, Weinberg RA, 2011. A perspective on cancer cell metastasis. *Science*, 331(6024):1559-1564.
https://doi.org/10.1126/science.1203543

Chen SH, Chen JM, Qin ZH, et al., 2024. Microfluidic thermotaxic selection of highly motile sperm and in vitro fertilization. *Bio-Design and Manufacturing*, 7(5):687-700.
https://doi.org/10.1007/s42242-024-00306-1

Cohen SJ, Alpaugh RK, Gross S, et al., 2006. Isolation and characterization of circulating tumor cells in patients with metastatic colorectal cancer. *Clinical Colorectal Cancer*, 6(2):125-132.
https://doi.org/10.3816/CCC.2006.n.029

Cortés-Hernández LE, Eslami-S Z, Pantel K, et al., 2020. Molecular and functional characterization of circulating tumor cells: from discovery to clinical application. *Clinical Chemistry*, 66(1):97-104.
https://doi.org/10.1373/clinchem.2019.303586

Cristofanilli M, Budd GT, Ellis MJ, et al., 2004. Circulating tumor cells, disease progression, and survival in metastatic breast cancer. *New England Journal of Medicine*, 351(8):781-791.
https://doi.org/10.1056/NEJMoa040766

de Bono JS, Scher HI, Montgomery RB, et al., 2008. Circulating tumor cells predict survival benefit from treatment in metastatic castration-resistant prostate cancer. *Clinical Cancer Research*, 14(19):6302-6309.
https://doi.org/10.1158/1078-0432.CCR-08-0872

Galletti G, Sung MS, Vahdat LT, et al., 2014. Isolation of breast cancer and gastric cancer circulating tumor cells by use of an anti HER2-based microfluidic device. *Lab on a Chip*, 14(1):147-156.
https://doi.org/10.1039/c3lc51039e

Havers M, Broman A, Lenshof A, et al., 2023. Advancement and obstacles in microfluidics-based isolation of extracellular vesicles. *Analytical and Bioanalytical Chemistry*, 415(7):1265-1285.
https://doi.org/10.1007/s00216-022-04362-3

Hu JR, Ren A, Lv WK, et al., 2025. Multiphoton polymerization-based micro/nanomanufacturing toward precision medicine. *Engineering*, 49:35-60.
https://doi.org/10.1016/j.eng.2024.10.016

Kang HY, Xiong YT, Ma L, et al., 2022. Recent advances in micro-/nanostructure array integrated microfluidic devices for efficient separation of circulating tumor cells. *RSC Advances*, 12(54):34892-34903.
https://doi.org/10.1039/D2RA06339E

Kang HY, Li C, Liu WF, et al., 2025. Si nanorod array integrated microfluidic device for enhanced extracellular

vesicle isolation. *Advanced Materials Technologies*, 10(1): 2400294. https://doi.org/10.1002/admt.202400294

Kang YT, Doh I, Byun J, et al., 2017. Label-free rapid viable enrichment of circulating tumor cell by photosensitive polymer-based microfilter device. *Theranostics*, 7(13): 3179-3191. https://doi.org/10.7150/thno.19686

Li C, Chen TN, 2005. Simulation and optimization of chaotic micromixer using lattice Boltzmann method. *Sensors and Actuators B: Chemical*, 106(2):871-877. https://doi.org/10.1016/j.snb.2004.09.006

Li HX, Qiao Y, Dai XL, et al., 2024. 3D bioprinting of tumor models and potential applications. *Bio-Design and Manufacturing*, 7(6):857-888. https://doi.org/10.1007/s42242-024-00317-y

Lin Y, He DL, Wu ZR, et al., 2023. Junction matters in hydraulic circuit bio-design of microfluidics. *Bio-Design and Manufacturing*, 6(1):38-50. https://doi.org/10.1007/s42242-022-00215-1

Liu Q, Mille LS, Villalobos C, et al., 2023. 3D-bioprinted cholangiocarcinoma-on-a-chip model for evaluating drug responses. *Bio-Design and Manufacturing*, 6(4):373-389. https://doi.org/10.1007/s42242-022-00229-9

Liu XS, Ma L, Yan WY, et al., 2022. A review of recent progress toward the efficient separation of circulating tumor cells via micro-/nanostructured microfluidic chips. *VIEW*, 3(1):20210013. https://doi.org/10.1002/VIW.20210013

Low WS, Abas WABW, 2015. Benchtop technologies for circulating tumor cells separation based on biophysical properties. *Biomed Research International*, 2015:239362. https://doi.org/10.1155/2015/239362

Ma L, Yang HY, 2023. What's next toward the bio-design and manufacturing field? *Bio-Design and Manufacturing*, 6(6): 735-741. https://doi.org/10.1007/s42242-023-00260-4

Park ES, Jin C, Guo Q, et al., 2016. Continuous flow deformability-based separation of circulating tumor cells using microfluidic ratchets. *Small*, 12(14):1909-1919. https://doi.org/10.1002/smll.201503639

Renier C, Pao E, Che J, et al., 2017. Label-free isolation of prostate circulating tumor cells using Vortex microfluidic technology. *npj Precision Oncology*, 1(1):15. https://doi.org/10.1038/s41698-017-0015-0

Rosenberg R, Gertler R, Friederichs J, et al., 2002. Comparison of two density gradient centrifugation systems for the enrichment of disseminated tumor cells in blood. *Cytometry*, 49(4):150-158. https://doi.org/10.1002/cyto.10161

Salafi T, Zhang Y, Zhang Y, 2019. A review on deterministic lateral displacement for particle separation and detection. *Nano-Micro Letters*, 11(1):77. https://doi.org/10.1007/s40820-019-0308-7

Santana SM, Antonyak MA, Cerione RA, et al., 2014. Microfluidic isolation of cancer-cell-derived microvesicles from hetergeneous extracellular shed vesicle populations. *Biomedical Microdevices*, 16(6):869-877. https://doi.org/10.1007/s10544-014-9891-z

Sarioglu AF, Aceto N, Kojic N, et al., 2015. A microfluidic device for label-free, physical capture of circulating tumor cell clusters. *Nature Methods*, 12(7):685-691. https://doi.org/10.1038/NMETH.3404

Sheng WA, Chen T, Tan WH, et al., 2013. Multivalent DNA nanospheres for enhanced capture of cancer cells in microfluidic devices. *ACS Nano*, 7(8):7067-7076. https://doi.org/10.1021/nn4023747

Shi JJ, Zhao CQ, Shen MQ, et al., 2022. Combination of microfluidic chips and biosensing for the enrichment of circulating tumor cells. *Biosensors and Bioelectronics*, 202: 114025. https://doi.org/10.1016/j.bios.2022.114025

Shu Y, Li B, Ma HL, et al., 2024. Three-dimensional breast cancer tumor models based on natural hydrogels: a review. *Journal of Zhejiang University-SCIENCE B*, 25(9): 736-755. https://doi.org/10.1631/jzus.B2300840

Smerage JB, Barlow WE, Hortobagyi GN, et al., 2014. Circulating tumor cells and response to chemotherapy in metastatic breast cancer: SWOG S0500. *Journal of Clinical Oncology*, 32(31):3483-3489. https://doi.org/10.1200/JCO.2014.56.2561

Stroock AD, Dertinger SKW, Ajdari A, et al., 2002. Chaotic mixer for microchannels. *Science*, 295(5555):647-651. https://doi.org/10.1126/science.1066238

Sun N, Yang YY, Miao H, et al., 2022. Discovery and characterization of circulating tumor cell clusters in neuroendocrine tumor patients using nanosubstrate-embedded microchips. *Biosensors and Bioelectronics*, 199:113854. https://doi.org/10.1016/j.bios.2021.113854

Sung H, Ferlay J, Siegel RL, et al., 2021. Global cancer statistics 2020: GLOBOCAN estimates of incidence and mortality worldwide for 36 cancers in 185 countries. *CA: A Cancer Journal for Clinicians*, 71(3):209-249. https://doi.org/10.3322/caac.21660

Varmazyari V, Habibiyan H, Ghafoorifard H, et al., 2022. A dielectrophoresis-based microfluidic system having double-sided optimized 3D electrodes for label-free cancer cell separation with preserving cell viability. *Scientific Reports*, 12(1):12100. https://doi.org/10.1038/s41598-022-16286-0

Wu MX, Huang PH, Zhang R, et al., 2018. Circulating tumor cell phenotyping via high-throughput acoustic separation. *Small*, 14(32):1801131. https://doi.org/10.1002/smll.201801131

Wu MR, Gao Y, Luan QY, et al., 2023. Three-dimensional lab-on-a-foil device for dielectrophoretic separation of cancer cells. *Electrophoresis*, 44(23):1802-1809. https://doi.org/10.1002/elps.202200287

Xiang N, Wang J, Li Q, et al., 2019. Precise size-based cell separation via the coupling of inertial microfluidics and deterministic lateral displacement. *Analytical Chemistry*, 91(15):10328-10334. https://doi.org/10.1021/acs.analchem.9b02863

Xie YL, Rufo J, Zhong RY, et al., 2020. Microfluidic isolation and enrichment of nanoparticles. *ACS Nano*, 14(12):

16220-16240.
https://doi.org/10.1021/acsnano.0c06336

Yu XL, He RX, Li SS, et al., 2013. Magneto-controllable capture and release of cancer cells by using a micropillar device decorated with graphite oxide-coated magnetic nanoparticles. *Small*, 9(22):3895-3901.
https://doi.org/10.1002/smll.201300169

Zeming KK, Ranjan S, Zhang Y, 2013. Rotational separation of non-spherical bioparticles using I-shaped pillar arrays in a microfluidic device. *Nature Communications*, 4(1):1625.
https://doi.org/10.1038/ncomms2653

Zhang NG, Deng YL, Tai QD, et al., 2012. Electrospun TiO_2 nanofiber-based cell capture assay for detecting circulating tumor cells from colorectal and gastric cancer patients. *Advanced Materials*, 24(20):2756-2760.
https://doi.org/10.1002/adma.201200155

Zhang TL, Hong ZY, Tang SY, et al., 2020. Focusing of submicrometer particles in microfluidic devices. *Lab on a Chip*, 20(1):35-53.
https://doi.org/10.1039/c9lc00785g

Zhang YZ, Wang ZY, Wu L, et al., 2018. Combining multiplex SERS nanovectors and multivariate analysis for in situ profiling of circulating tumor cell phenotype using a microfluidic chip. *Small*, 14(20):1704433.
https://doi.org/10.1002/smll.201704433

Zhang ZM, Henry E, Gompper G, et al., 2015. Behavior of rigid and deformable particles in deterministic lateral displacement devices with different post shapes. *The Journal of Chemical Physics*, 143(24):243145.
https://doi.org/10.1063/1.4937171

Zhou JH, Rossi J, 2017. Aptamers as targeted therapeutics: current potential and challenges. *Nature Reviews Drug Discovery*, 16(3):181-202.
https://doi.org/10.1038/nrd.2016.199

Electronic supplementary materials

Figs. S1–S3